HHS Public Access

Author manuscript

Nat Cell Biol. Author manuscript; available in PMC 2014 November 01.

Published in final edited form as:

Nat Cell Biol. 2014 May ; 16(5): 479–485. doi:10.1038/ncb2939.

Structural mechanism of the dynein powerstroke

Jianfeng Lin[1], **Kyoko Okada**[1], **Milen Raytchev**[1], **Maria C. Smith**[1], and **Daniela Nicastro**[1,2]

[1] Biology Department and Rosenstiel Basic Medical Sciences Research Center, Brandeis University, Waltham, Massachusetts 02454-9110, USA

Abstract

Dyneins are large microtubule motor proteins required for mitosis, intracellular transport, and ciliary and flagellar motility[1,2]. They generate force through a powerstroke mechanism, which is an ATP-consuming cycle of pre- and post-powerstroke conformational changes that cause relative motion between different dynein domains[3-5]. However, key structural details of dynein's force generation remain elusive. Here, using cryo-electron tomography of intact, active (i.e. beating), rapidly frozen, sea urchin sperm flagella, we determined the *in situ* 3D structures of all domains of both pre- and post-powerstroke dynein, including the previously unresolved linker and stalk of pre-powerstroke dynein. Our results reveal that the rotation of the head relative to the linker is the key action in dynein movement, and that there are at least two distinct pre-powerstroke conformations: pre-I (microtubule-detached) and pre-II (microtubule-bound). We provide 3D-reconstructions of native dyneins in three conformational states, *in situ*, allowing us to propose a molecular model of the structural cycle underlying dynein movement.

Dyneins are minus-end directed motors that use conformation-dependent changes associated with ATP-binding and hydrolysis to attach to and walk along microtubules[1-5]. Dyneins are categorised into two functional classes: axonemal and cytoplasmic[1]. Axonemal dyneins are arranged in a repeating pattern along the microtubular cytoskeleton of cilia and flagella, and power the sliding motions between outer doublet microtubules to drive ciliary and flagellar motility[6,7] (Fig. 1); cytoplasmic dyneins function as individual homodimers and transport diverse intracellular cargoes along microtubules[1]. Dysfunction of dynein causes devastating conditions in humans, including ciliopathies and neurodegenerative diseases[8,9].

[2] Correspondence should be addressed to D. N. (nicastro@brandeis.edu).

Accession numbers

Cryo-ET structural data have been deposited in the Electron Microscopy Data Bank (primary accessions: EMD-5757 and EMD-5758) and the corresponding fitted atomic coordinates have been deposited in the Protein Data Bank (primary accessions: 3J67 and 3J68; referenced accession used to generate 3J67 and 3J68 is 4AKI).

Author Contributions

D.N. conceived and directed the study. J.L. performed the experiments. J.L., M.R. and D.N. analysed the data. J.L., K.O., M.C.S. and D.N. wrote the manuscript.

Note: Supplementary Information is available in the online version of the paper.

Competing financial interests

The authors declare no competing financial interests.

The structural mechanisms that underlie dynein movement, and therefore function, are not completely understood. Dynein motility is generated by a conserved motor domain that contains a ring-shaped head with six AAA-domains, a coiled-coil stalk with a microtubule binding domain (MTBD) at its tip, and the linker, which connects on its C-terminal end with the ATP-hydrolysing AAA1-domain and on its N-terminal end with the cargo-binding tail (Fig. 1a)[10-14]. To move cargo along microtubule-tracks, dyneins generate force through an ATP-consuming powerstroke, which is preceded and followed by pre- and post-powerstroke conformational changes, respectively[3-5]. Previous 2D negative-stain electron microscopy (EM) studies of isolated dynein, in the absence of microtubules, visualised two conformational states (primed and unprimed), which are thought to represent the pre- and post-powerstroke forms[15,16]. Subsequent cryo-EM and tomography studies determined 3D structures of dynein[17,18], but did not resolve key motor subdomains, e.g. the stalk and linker, in the pre-powerstroke state(s). Recent studies revealed the crystal structure of the motor domain of truncated dynein in the post-powerstroke state[10-12]. However, a complete understanding of dynein's motility mechanism requires 3D visualisation of the different conformational states adopted by native dyneins throughout their mechanochemical cycle, under physiological conditions and in their cellular context with both microtubule-tracks and cargo present. Here we present the most complete set of structures, to date, of the conformational cycle of native dyneins in their cellular context.

The characteristic, oscillatory beating of cilia and flagella is driven by the activity of thousands of precisely, spatio-temporally regulated dyneins. We and others have previously shown that cryo-electron tomography (cryo-ET) and subtomogram averaging of inactive flagella can provide 3D structures of macromolecular complexes, including dyneins in their post-powerstroke (“inactive”) state, with 3-5 nm resolution[19]. Flagellar dyneins are organised into two rows, the outer and inner dynein arms (ODA and IDA) that repeat periodically along the nine doublet microtubules that form the axonemal core of cilia and flagella; each doublet microtubule is composed of 96-nm-long axonemal repeat units (Fig. 1b-d)[1,2,20]. To visualise these dyneins, not only in their post-powerstroke state, but in different conformations throughout their mechanochemical cycle, we used cryo-ET to image intact flagella from sea urchin (*Strongylocentrotus purpuratus*) sperm that had been rapidly frozen while actively beating (Supplementary Video 1), which trapped the dyneins (within milliseconds) in different conformations along the sinusoidally-bent flagella. A powerful technique to improve the resolution of the 3D reconstructions of axonemal complexes is subtomogram averaging of the 96 nm axonemal repeats[19]; the repeat units were extracted from the raw tomograms, aligned to one another in 3D and averaged. However, to preserve biologically meaningful structural differences between dyneins in different conformations it was important to use classification tools[21] that separated the many 3D maps of individual complexes into homogeneous (same conformation) sub-groups that were then combined into class-averages. Mapping the class-assignment of each repeat unit back to its location in the raw tomogram showed a highly-specific distribution of classes along the flagellar axonemes (Supplementary Fig. 1); this is consistent with regulated dynein activity driving flagellar motility and suggests that the automated classification resulted in a meaningful separation of specific functional dynein states. Class-averages that clearly visualised all major domains of dynein (resolutions between 3.0-4.8 nm; Supplementary Table 1) were subsequently used to

determine the key structural differences between different dynein conformations (Figs 3 and 4). As both a control and to re-investigate the structure of post-powerstroke dynein at high-resolution, we also imaged flagella from sea urchin sperm that were either inactivated using an ATPase inhibitor[22] (Supplementary Video 2) or demembranated to wash away nucleotides. Samples from either preparation were processed independently, but resulted in identical post-powerstroke dynein reconstructions for the different dynein isoforms (e.g., α-ODA, β-ODA, etc.); the post-powerstroke structures with the best resolutions are shown in Figures 2-4 (Supplementary Table 1). Demembranated (nucleotide-free) axonemes from the unicellular algae *Chlamydomonas reinhardtii* were also analysed to compare the post-powerstroke axonemal dyneins and conservation of structural features among evolutionarily distant species (Supplementary Fig. 2). To determine the interactions of the linker with other regions of the motor domain, we docked the recently published post-powerstroke crystal structures[12] into our 3D class-averages and identified the position of the linker relative to the six AAA-domains in different conformations (Figs 3h,j and 4b,d).

In most post-powerstroke dyneins, the N-terminus of the linker (distant from AAA1) latched onto the AAA4 and AAA5 domains close to the base of the stalk (Figs 2,3a-c,g,h, and 4a,b), as expected from previous studies[11,12,15,17]. In addition to confirming results from prior studies, we also identified previously undetected small, but conserved (from algae to sea urchin) differences between ODA and IDA structures (Fig. 2; Supplementary Fig. 2). Specifically, the head and stalk of IDAs were rotated slightly more counter-clockwise relative to the linker as compared to ODAs, such that the IDA linker-neck region is even closer to the stalk base and the angle of the stalk relative to the microtubule-track is steeper (~70° for IDA versus ~60° for ODA) (compare Fig. 2b-d',i with e-g',j; Supplementary Fig. 2b-e',j with f-h',k). The differences observed in the post-powerstroke conformations of different dynein isoforms may be due to spatial constraints between the complexes in the axoneme or to intrinsically different functions of the dyneins. A similar positional difference in the linker was observed between the crystal structures of cytoplasmic dyneins from both *Saccharomyces cerevisiae* and *Dictyostelium discoideum*, and is thought to be induced by ADP, as the two crystal structures were obtained in either the absence or presence of ADP[11,12]. Since nucleotides were removed from our axoneme samples, our data suggest that distinct dynein isoforms can exhibit at least two different apo-(nucleotide-free) conformations.

Our analysis of active flagella not only determined the high-resolution, 3D structure of full-length, pre-powerstroke dynein, but also revealed structures for two different pre-powerstroke conformations, which we termed the pre-I and pre-II states (Fig. 3d-f,i,j). Similar to the post-powerstroke state, we also found small differences between the ODA and IDA pre-powerstroke conformations. To analyse the structural differences between the observed dynein conformations, we superimposed the cargo-binding site of the tails of all class-averages and compared the positions and orientations of all major domains (Fig. 3a-f,h,j). We found that in all observed pre-powerstroke conformations the dynein head had swung towards the minus-end of the microtubule-track, pivoting around a point at the C-terminal end of the linker (close to AAA1), which effectively moved the stalk several nanometres towards the microtubule minus-end as compared to the post-powerstroke

structure. In contrast to the head and stalk, the pre-powerstroke neck-linker region did not significantly move relative to the microtubule, when compared to the post-powerstroke state (Fig. 3b,e,h,j); only the angle of the linker changed in some cases, e.g. the linker of ODAs was more parallel to the microtubule axis in the pre-powerstroke state (Fig. 3e,j). The relative motion between the rotating head and the more-or-less stationary linker resembled an opening jack-knife with an angular amplitude of ~65°, and altered the interactions between the linker and head domains. The C-terminal half of the ODA linker that is positioned close to domains AAA1 and AAA6 in the post-powerstroke conformation, interacts with domains AAA1 and AAA2 in the pre-powerstroke state, whereas the N-terminal half of the linker that is located close to the stalk base in the post-powerstroke state protrudes from the head domain in the pre-powerstroke conformation (compare Fig. 3b,h with 3e,j). This large distance between the linker and the base of the stalk in our 3D pre-powerstroke structures is consistent with previous 2D negative-stain images of isolated dynein in a nucleotide-bound, “primed” state[15].

Overall, the IDAs showed the same structural changes between post- and pre-powerstroke conformations with only small differences: the angle of the IDA linker remained even more stationary between different conformations than the ODA linker; the angular amplitude of the IDA head rotation relative to the linker, as it changed from a post- to pre-powerstroke conformation, was slightly smaller (~50°). Therefore, the interaction of the N-terminal side of the linker with the head changed from AAA5 in the post-powerstroke to AAA3 and AAA2 in the pre-powerstroke state (Fig. 4; Supplementary Fig. 3). Our comparison of dynein conformations suggests that rotation of the ring-shaped head relative to the more static linker is the key action of the recovery (priming) stroke (post- to pre-powerstroke transition) and the powerstroke (pre- to post-powerstroke transition), rather than major conformational changes in the linker or tail regions, as previously hypothesised[18,23].

Our classification revealed two different pre-powerstroke conformations of the ODAs, the pre-I and pre-II states. Although the head was rotated into the “primed” forward position in both states, in pre-I, the stalk was detached with the MTBD located a few nanometres above the microtubule-track (Fig. 3d; α-ODA), while in pre-II, the stalk was microtubule-bound (Fig. 3f; β-ODA). For the MTBD to reach the microtubule-track, the pre-II head and stalk are tilted ~20° counter-clockwise in comparison to pre-I (Fig. 3d,f). However, the linker-head interactions appeared unchanged between the two pre-powerstroke states, because the rotation was compensated for by bending in the neck-region (Fig. 3d-f,j). The 3D structure of the microtubule-detached pre-I conformation, including its stalk and MTBD, was remarkably well-resolved. A reconstruction with this clarity would likely be unfeasible using an *in vitro* system due to diffusion of the detached head, but was made possible here through the structural scaffold provided by intact flagella; i.e. the pre-I dyneins were held in place (instead of diffusing in space) by their tails anchoring to the cargo-microtubule and other domains contacting neighbouring axonemal structures.

The pre-I conformation (with primed linker and detached stalk) likely follows the post-powerstroke state, but precedes pre-II with a re-attached MTBD. This is supported by different amounts of movement of the dynein heads towards the microtubule minus-end in the pre- and post-powerstroke states; between the pre-I and post-powerstroke structures, the

head was shifted slightly less than 8 nm towards the microtubule minus-end (compare Fig. 3a and d), while between the pre-II and post-powerstroke states the shift was 8 nm (compare Fig. 3c and f), which is the most frequently observed step size of load-carrying dynein[24,25]. This is consistent with a previous 2D EM study of isolated sea urchin ODAs re-bound to microtubules *in vitro* that measured different shifts between dynein heads[23]. In sea urchin flagella, two dynein heavy chains, α- and β-dynein, form a dimeric ODA complex. Our classification of dyneins from active flagella revealed that the α-ODA was in the pre-I and the β-ODA in the pre-II state in more than 90% of the classified ODA dimers. This could be due to distinct roles of different ODA isoforms in axonemal motility generation, as suggested by previous studies[7,26]. Nonetheless, it indicates that the β-ODA predominates as the leading "leg" as this dimeric ODA complex walks along the microtubule-track in an inchworm fashion; this is similar to cytoplasmic dynein[27], but different from the "hand-over-hand" stepping characteristic of kinesins[28], the other molecular motors that walk along microtubules.

Previous studies have proposed a linker-swing model for dynein movement, mainly based on images of isolated dynein[11,16,17]. Here, we directly visualised 3D structures of both the pre-powerstroke linker and various dynein conformations in the presence of microtubule-track and cargo. We demonstrate that the linker remained remarkably stationary between post- and pre-powerstroke structures, while a rotation of the head domain, i.e. a "head-swing mechanism", appears to cause the major movement of dyneins relative to the microtubule (Figs 3 and 4; Supplementary Fig. 3). Previous studies predicted that a narrow cleft in the linker might be the hinge point for the swing of the linker relative to the head[11,12]. We simulated the swing around a pivot point using the published *S. cerevisiae* crystal structure and by cutting the linker at a proximal site close to the proposed hinge-like cleft[12], to then rotate the C-terminal regions of the dynein to the different positions suggested by our 3D conformational structures (Supplementary Fig. 4). The simulated maps closely resemble the reconstructed *in situ* conformations of flagellar dyneins, but we cannot exclude the possibility that the proximal linker region undergoes (additional) remodelling during the head swing.

The presence of microtubule tracks and cargo in the intact flagella allowed visualisation of previously unresolved conformational changes, including differences in the stalk structures. Our two most-clearly resolved dynein species, β-ODA and IDA a, showed that the stalk was bent in opposite directions between the pre-II and post-powerstroke states (Figs 3c,f and 4a,c). It is possible that these structural differences are due to flexibility in the coiled-coil stalk, i.e., the stalk is passively moved in different directions when it is subjected to changing forces during the mechanochemical cycle of dynein. Alternatively, these differences could correspond to distinct functional states of the stalk MTBD, i.e. opposite bends of the coiled-coil stalk could cause changes in the registration between the two helices of the coiled-coil stalk and thus of the microtubule binding affinity of the MTBD[4,13].

Along with a comprehensive understanding of the mechanochemical powerstroke cycle, we have visualised two previously undetected electron densities, directly attached to the dynein motor domain (Fig. 4; Supplementary Figs 2 and 3; white arrowheads). A likely candidate for one of these densities is the lissencephaly protein, Lis1, which is the only cofactor

known to directly interact with and modulate the activity of the dynein motor domain[29,30]. A single particle cryo-EM reconstruction of Lis1 bound to cytoplasmic dynein *in vitro* showed that Lis1 interacts with the AAA3 and AAA4 domains of dynein[29]. We observed an extra density attached to the AAA3 domain and the neck region of the tail of the post-powerstroke α-ODA in *Chlamydomonas* axonemes (Supplementary Fig. 2, white arrowheads). Lis1 was previously shown to associate with α-ODA in *Chlamydomonas* axonemes[30], making it a likely candidate for the extra density detected in our study. Although this extra density was not observed in sea urchin sperm flagella, another density was observed to be specifically attached to the linker, AAA1 and AAA2 of sea urchin pre-powerstroke IDA dyneins a, b, c, and e (Fig. 4c,d; Supplementary Fig. 3c,d, white arrowheads). Since AAA1 is the essential ATP hydrolysis site for the powerstroke, this extra density could be an isoform-specific regulator involved in the dynein powerstroke mechanism. Further studies are required to identify and functionally characterise these densities. Nonetheless, our findings emphasise that different dynein isoforms function in unique ways by employing distinct regulatory mechanisms.

Combined with previous kinetic studies[3-5], our structural data support the following model of dynein movement (Fig. 5; Supplementary Video 3): In the absence of nucleotides, a post-powerstroke conformation exists with the N-terminus of the linker attached to AAA4 or AAA5 (depending on the dynein isoform); the stalk is tightly bound to the microtubule-track with a 60°-70° angle relative to the microtubule (Fig. 5a). ATP binding to AAA1 of the head domain causes conformational changes that result in weakening of the microtubule affinity of the MTBD and its dissociation from the microtubule track. Following or concomitant with this dissociation, dynein undergoes a recovery stroke to the pre-powerstroke conformation pre-I by rotating the head and stalk clockwise (50°-70°). This moves the dynein head towards the microtubule minus-end and the dynein is now “primed” for a powerstroke (Fig. 5b). During or after ATP hydrolysis, the motor domain transitions from the pre-I to pre-II state (Fig. 5c) by tilting the head, together with the stalk, counter-clockwise such that the MTBD can re-bind (weakly) to a new binding site on the microtubule-track, closer to the minus-end. Upon release of phosphate, dynein once again binds strongly to the microtubule. The powerstroke brings the linker again close to the stalk base, like a closing jack-knife, and into the post-powerstroke position, while the tail and bound cargo are pulled towards the new binding site (Fig. 5d). The stalk serves as a tether to the microtubule, while the cargo is “winched” towards the microtubule minus-end. Upon release of ADP from the dynein, a new mechanochemical cycle begins.

In summary, we highlight three key findings: 1) the priming recovery stroke is mainly achieved by rotation of the head domain with respect to the more-or-less stationary linker, rather than shifting of the head through remodelling of the linker and/or tail, 2) during dynein stepping, different sites of the linker interact with various AAA domains of the head, and 3) by visualising the 3D structure of full-length dynein in multiple conformations we can propose a mechanistic model that shows how conformational changes of different domains are coordinated and coupled with ATP hydrolysis to achieve cyclical dynein movement. Overall, our study provides insights into the structural changes that govern

dynein movement under physiological conditions and establishes an improved platform upon which to continue studies of dynein *in situ*.

Methods

Cryo-sample preparation

Live sea urchins (*Strongylocentrotus purpuratus*) were purchased from Monterey Abalone Co. (Monterey, CA). Spawning was induced by the injection of 1-2 ml of 0.5 M KCl into the perivisceral cavity[32]. Sperm samples were collected from adult male sea urchins and divided to prepare three different types of sample: (part A) active sperm, (part B) ATPase-inhibited sperm, and (part C) isolated axonemes. Prior to preparation, inclusion criteria required: live and active (beating) sea urchin sperm flagella. Sperm were diluted in artificial seawater (360 mM NaCl, 50 mM $MgCl_2$, 10 mM $CaCl_2$, 10 mM KCl, 30 mM HEPES, pH 8.0), and the motility was imaged using the DIC mode of a Marianas spinning disk confocal system (3I, Denver, CO) consisting of a Zeiss Observer Z1 microscope (Carl Zeiss, Jena, Germany) equipped with a Yokagawa CSU-X1 spinning disk confocal head (Yokogawa, Tokyo, Japan) and a QuantEM 512SC EMCCD camera (Photometrics, Tucson, AZ). All harvested cells were active and no samples were excluded. Immediately following motility confirmation, Part A (active sperm that were diluted in artificial seawater, Supplementary Video 1), was rapidly frozen (as described below). Part B was diluted in artificial seawater containing the ATPase inhibitor erythro-9-[3-(2-hydroxynonyl)]-adenine (EHNA, 2 mM)[22]; after a five minute incubation at ~16 °C, the sample was imaged at the light microscope to confirm that sperm were completely immotile (Supplementary Video 2), and they were then rapidly frozen. Part C was diluted in demembranation buffer (30 mM HEPES, pH 8.0, 150 mM KCl, 4 mM $MgCl_2$, 0.5 mM EGTA, 0.1% Triton X-100) to remove the flagellar membrane. After a one minute incubation, the sperm were collected by centrifugation, resuspended in demembranation buffer (without Triton X-100), and rapidly frozen.

Chlamydomonas reinhardtii axonemes were isolated from a pseudo wild-type (pWT) strain (pf2-4::PF2-GFP), as previously described[33]. The pWT strain is a rescued mutant and is structurally and phenotypically indistinguishable from WT. Flagella were detached from the cells using the pH-shock method[34], and purified by two centrifugation steps at 2,400 × g, for 10 min, at 4°C with a 20% sucrose cushion. Purified flagella were demembranated with 0.1 % IGEPAL CA-630 (Sigma-Aldrich, St. Louis, MO) and axonemes were collected by centrifugation at 35,000 × g, for one hour at 4°C. The axoneme pellet was washed, resuspended in HMEEN buffer (30 mM HEPES, pH 7.4, 5 mM $MgSO_4$, 1 mM EGTA, 0.1 mM EDTA, 25 mM NaCl, and 0.1 μg/ml aprotinin, leupeptin, and pepstatin), and rapidly frozen.

Sperm and axoneme samples were rapidly frozen on Quantifoil holey carbon grids (Quantifoil Micro Tools GmbH, Germany) that were glow discharged, coated with 10 nm colloidal gold (Sigma-Aldrich), and loaded on a homemade plunge freezing device. Sample (3 μl) and fivefold concentrated 10 nm colloidal gold solution (1 μl)[35] were applied to the grid. The grid was blotted with filter paper for 1.5 - 2.5 seconds and immediately frozen by plunging into liquid ethane. The vitrified samples were then stored in liquid nitrogen until examined by EM.

Cryo-electron tomography

Tilt series acquisitions and tomogram reconstructions were conducted as previously described[33,36]. In brief, cryo-samples were imaged at 300 keV, with -6 μm or -8 μm defocus, under low-dose conditions and with an energy filter (Gatan, Pleasanton, CA) in zero-loss mode (20 eV slit width) on a Tecnai F30 transmission electron microscope (FEI, Hillsboro, OR). Electron tomography data were only recorded for flagella that appeared well-preserved by EM inspection. Tilt series were recorded while stepwise rotating the sample from approximately −65 to +65° with 1.5 - 2.5° angular increments, using the SerialEM image acquisition software[37]. The cumulative electron dose per tilt series was limited to ~100 e/Å^2 to avoid radiation damage. All images were recorded on a 2k×2k charge-coupled device camera (Gatan, Pleasanton, CA) at a nominal magnification of 13,500, resulting in a pixel size of ~1 nm.

Image processing

The tilt series images were first aligned using the 10 nm gold particles as fiducial markers, and then reconstructed by weighted back-projection into tomograms using the IMOD software[38]. The *Chlamydomonas* tomograms were previously utilised for the analysis of other axonemal complexes[33]. Tomographic reconstructions with compressed flagella (caused by embedding in too thin ice during cryo-sample preparation) or insufficient fiducial markers for alignment were excluded from subtomogram averaging and analysis. The 96 nm axonemal repeat units along the doublet microtubules were extracted from the raw tomograms, aligned (volume size, 110 × 84 × 80 nm), and averaged (including missing wedge compensation) using the program PEET[20] to obtain sub-tomogram averages with enhanced signal-to-noise ratio and improved resolution. To obtain structures with consistent conformations, we further performed automated classification on the aligned sub-tomograms from sea urchin sample A (sperm frozen while actively beating), using a clustering approach (principle component analysis) built into the PEET program[21]. To focus the classification on different dynein isoforms of interest, appropriate masks were applied prior to classification. Subtomograms that contain the dynein of interest in the same state were grouped into the same class and were averaged using the original alignment to generate a class-average; masks were only used for the classifications, but not for alignment or averaging. The resolution of the resulting averages was estimated in a (20 nm)^3 sub-volume in the centre of interest using the 0.5 criterion of the Fourier shell correlation method[39]. The number of tomograms, and both particle numbers and resulting resolutions are reported in Supplementary Table 1, for each sample. The crystal structure fitting and 3D visualisation by isosurface rendering were carried out using the UCSF Chimera program[40]. To generate the simulated density maps of dynein in different conformational states, the linker was cut at the proposed linker-swing hinge site from the crystal structure of *S. cerevisiae* (yeast) cytoplasmic dynein (PDB 4AKI A chain)[12], and the N-terminal linker part (between hinge and tail) was rotated around the hinge point to the locations predicted by our cryo-ET structures. The density maps were generated from these modified crystal structures using the Chimera *molmap* command.

Supplementary Material

Refer to Web version on PubMed Central for supplementary material.

Acknowledgements

We thank Daniel T.N. Chen (Brandeis University) for providing *Strongylocentrotus purpuratus* sperm; Mary Porter (University of Minnesota) for providing the pWT *Chlamydomonas* strain; Chen Xu for providing training and management of the Brandeis EM facility. We are grateful to David Mitchell (SUNY Upstate Medical University), and Jeff Gelles, David DeRosier and Thomas Heuser (all from Brandeis University) for critically reading the manuscript. This work was supported by funding from the National Institutes of Health (GM083122 to DN).

References

1. Hook P, Vallee RB. The dynein family at a glance. J. Cell Sci. 2006; 119:4369–4371. [PubMed: 17074830]
2. Gibbons IR, Rowe AJ. Dynein: A Protein with Adenosine Triphosphatase Activity from Cilia. Science. 1965; 149:424–426. [PubMed: 17809406]
3. Johnson KA. Pathway of the microtubule-dynein ATPase and the structure of dynein: a comparison with actomyosin. Annu. Rev. Biophys. Biophys. Chem. 1985; 14:161–188. [PubMed: 3159394]
4. Kon T, et al. Helix sliding in the stalk coiled coil of dynein couples ATPase and microtubule binding. Nat. Struct. Mol. Biol. 2009; 16:325–333. [PubMed: 19198589]
5. Tsygankov D, Serohijos AW, Dokholyan NV, Elston TC. Kinetic models for the coordinated stepping of cytoplasmic dynein. J. Chem. Phys. 2009; 130
6. Summers KE, Gibbons IR. Adenosine triphosphate-induced sliding of tubules in trypsin-treated flagella of sea-urchin sperm. Proc. Natl Acad. Sci. USA. 1971; 68:3092–3096. [PubMed: 5289252]
7. King SM. Integrated control of axonemal dynein AAA(+) motors. J. Struct. Biol. 2012; 179:222–228. [PubMed: 22406539]
8. Fliegauf M, Benzing T, Omran H. When cilia go bad: cilia defects and ciliopathies. Nat. Rev. Mol. Cell Biol. 2007; 8:880–893. [PubMed: 17955020]
9. Eschbach J, Dupuis L. Cytoplasmic dynein in neurodegeneration. Pharmacol. Ther. 2011; 130:348–363. [PubMed: 21420428]
10. Cho C, Vale RD. The mechanism of dynein motility: insight from crystal structures of the motor domain. Biochim. Biophys. Acta. 2012; 1823:182–191. [PubMed: 22062687]
11. Kon T, et al. The 2.8 A crystal structure of the dynein motor domain. Nature. 2012; 484:345–350. [PubMed: 22398446]
12. Schmidt H, Gleave ES, Carter AP. Insights into dynein motor domain function from a 3.3-A crystal structure. Nat. Struct. Mol. Biol. 2012; 19:492–497. S1. [PubMed: 22426545]
13. Carter AP, et al. Structure and functional role of dynein's microtubule-binding domain. Science. 2008; 322:1691–1695. [PubMed: 19074350]
14. King SM. The dynein microtubule motor. Biochim. Biophys. Acta. 2000; 1496:60–75. [PubMed: 10722877]
15. Burgess SA, Walker ML, Sakakibara H, Knight PJ, Oiwa K. Dynein structure and power stroke. Nature. 2003; 421:715–718. [PubMed: 12610617]
16. Roberts AJ, et al. AAA+ Ring and linker swing mechanism in the dynein motor. Cell. 2009; 136:485–495. [PubMed: 19203583]
17. Roberts AJ, et al. ATP-driven remodeling of the linker domain in the dynein motor. Structure. 2012; 20:1670–1680. [PubMed: 22863569]
18. Movassagh T, Bui KH, Sakakibara H, Oiwa K, Ishikawa T. Nucleotide-induced global conformational changes of flagellar dynein arms revealed by in situ analysis. Nat. Struct. Mol. Biol. 2010; 17:761–767. [PubMed: 20453857]
19. Mizuno N, Taschner M, Engel BD, Lorentzen E. Structural studies of ciliary components. J. Mol. Biol. 2012; 422:163–180. [PubMed: 22683354]

20. Nicastro D, et al. The molecular architecture of axonemes revealed by cryoelectron tomography. Science. 2006; 313:944–948. [PubMed: 16917055]
21. Heumann JM, Hoenger A, Mastronarde DN. Clustering and variance maps for cryo-electron tomography using wedge-masked differences. J. Struct. Biol. 2011; 175:288–299. [PubMed: 21616153]
22. Bouchard P, Penningroth SM, Cheung A, Gagnon C, Bardin CW. erythro-9-[3-(2-Hydroxynonyl)]adenine is an inhibitor of sperm motility that blocks dynein ATPase and protein carboxylmethylase activities. Proc. Natl Acad. Sci. USA. 1981; 78:1033–1036. [PubMed: 6453342]
23. Ueno H, Yasunaga T, Shingyoji C, Hirose K. Dynein pulls microtubules without rotating its stalk. Proc. Natl Acad. Sci. USA. 2008; 105:19702–19707. [PubMed: 19064920]
24. Mallik R, Carter BC, Lex SA, King SJ, Gross SP. Cytoplasmic dynein functions as a gear in response to load. Nature. 2004; 427:649–652. [PubMed: 14961123]
25. Sakakibara H, Kojima H, Sakai Y, Katayama E, Oiwa K. Inner-arm dynein c of *Chlamydomonas* flagella is a single-headed processive motor. Nature. 1999; 400:586–590. [PubMed: 10448863]
26. Moss AG, Sale WS, Fox LA, Witman GB. The alpha subunit of sea urchin sperm outer arm dynein mediates structural and rigor binding to microtubules. J. Cell Biol. 1992; 118:1189–1200. [PubMed: 1387406]
27. Qiu W, et al. Dynein achieves processive motion using both stochastic and coordinated stepping. Nat. Struct. Mol. Biol. 2012; 19:193–200. [PubMed: 22231401]
28. Yildiz A, Tomishige M, Vale RD, Selvin PR. Kinesin walks hand-over-hand. Science. 2004; 303:676–678. [PubMed: 14684828]
29. Huang J, Roberts AJ, Leschziner AE, Reck-Peterson SL. Lis1 acts as a “clutch” between the ATPase and microtubule-binding domains of the dynein motor. Cell. 2012; 150:975–986. [PubMed: 22939623]
30. Rompolas P, Patel-King RS, King SM. Association of Lis1 with outer arm dynein is modulated in response to alterations in flagellar motility. Mol. Biol. Cell. 2012; 23:3554–3565. [PubMed: 22855525]
31. Linck RW, Stephens RE. Functional protofilament numbering of ciliary, flagellar, and centriolar microtubules. Cell Motil. Cytoskeleton. 2007; 64:489–495. [PubMed: 17366641]
32. Gibbons IR. Sliding and bending in sea urchin sperm flagella. Symp. Soc. Exp. Biol. 1982; 35:225–287. [PubMed: 6764041]
33. Heuser T, Raytchev M, Krell J, Porter ME, Nicastro D. The dynein regulatory complex is the nexin link and a major regulatory node in cilia and flagella. J. Cell Biol. 2009; 187:921–933. [PubMed: 20008568]
34. Witman GB, Carlson K, Berliner J, Rosenbaum JL. *Chlamydomonas* flagella. I. Isolation and electrophoretic analysis of microtubules, matrix, membranes, and mastigonemes. J. Cell Biol. 1972; 54:507–539. [PubMed: 4558009]
35. Iancu CV, et al. Electron cryotomography sample preparation using the Vitrobot. Nat. Protoc. 2006; 1:2813–2819. [PubMed: 17406539]
36. Lin J, Heuser T, Song K, Fu X, Nicastro D. One of the nine doublet microtubules of eukaryotic flagella exhibits unique and partially conserved structures. PLoS One. 2012; 7:e46494. [PubMed: 23071579]
37. Mastronarde DN. Automated electron microscope tomography using robust prediction of specimen movements. J. Struct. Biol. 2005; 152:36–51. [PubMed: 16182563]
38. Kremer JR, Mastronarde DN, McIntosh JR. Computer visualization of three-dimensional image data using IMOD. J. Struct. Biol. 1996; 116:71–76. [PubMed: 8742726]
39. Harauz G, Van Heel M. Exact filters for general geometry three dimensional reconstruction. Optik. 1986; 73:146–156.
40. Pettersen EF, et al. UCSF Chimera--a visualization system for exploratory research and analysis. J. Comput. Chem. 2004; 25:1605–1612. [PubMed: 15264254]

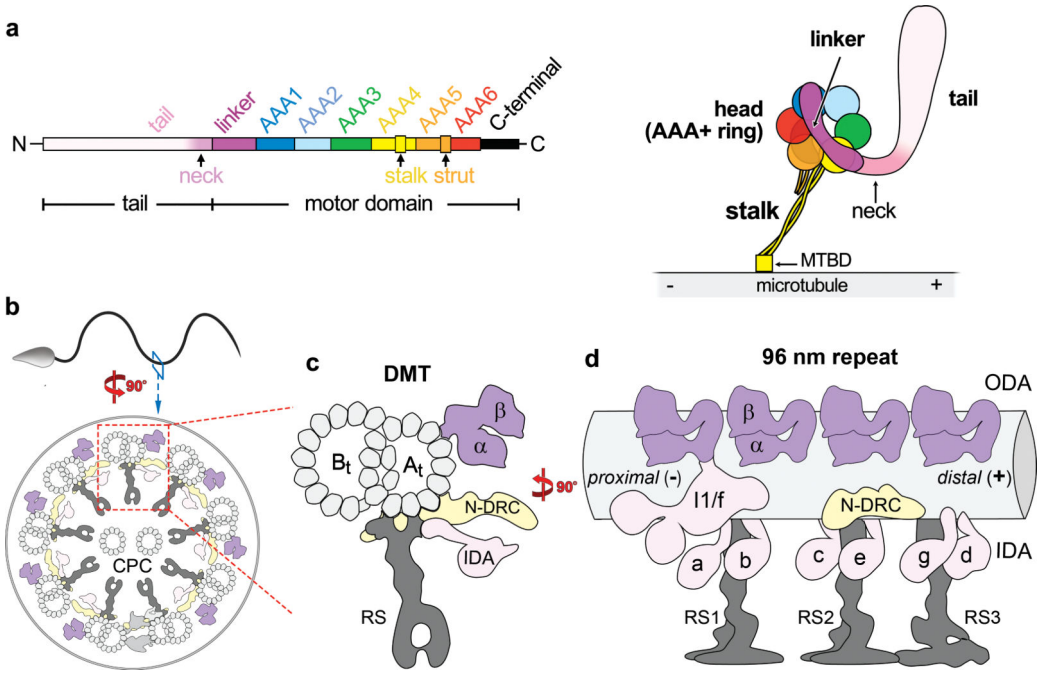

Figure 1.

Dynein and its arrangement in sea urchin sperm flagella. (**a**) Sequence diagram and schematic of domain organisation of one dynein heavy chain. (**b**) Diagrams of a sea urchin sperm cell (top) and its flagellum viewed in cross-section from the proximal side (bottom). (**c**) Diagram of an outer doublet microtubule (DMT) viewed in cross-section. (**d**) Diagram of a 96 nm long axonemal unit that repeats along the doublet microtubule; each repeat unit contains: four outer dynein arms (ODAs), six single-headed inner dynein arms (IDAs: a, b, c, d, e, and g, based on the nomenclature of *Chlamydomonas*), and one double-headed IDA (I1 or IDA f) anchored to the A-tubule (At) of the doublet microtubule. Other labels: B-tubule (B_t), central pair complex (*CPC*), nexin-dynein regulatory complex (*N-DRC*), radial spoke (*RS*), microtubule binding domain (*MTBD*), microtubule polarity (+ and - end).

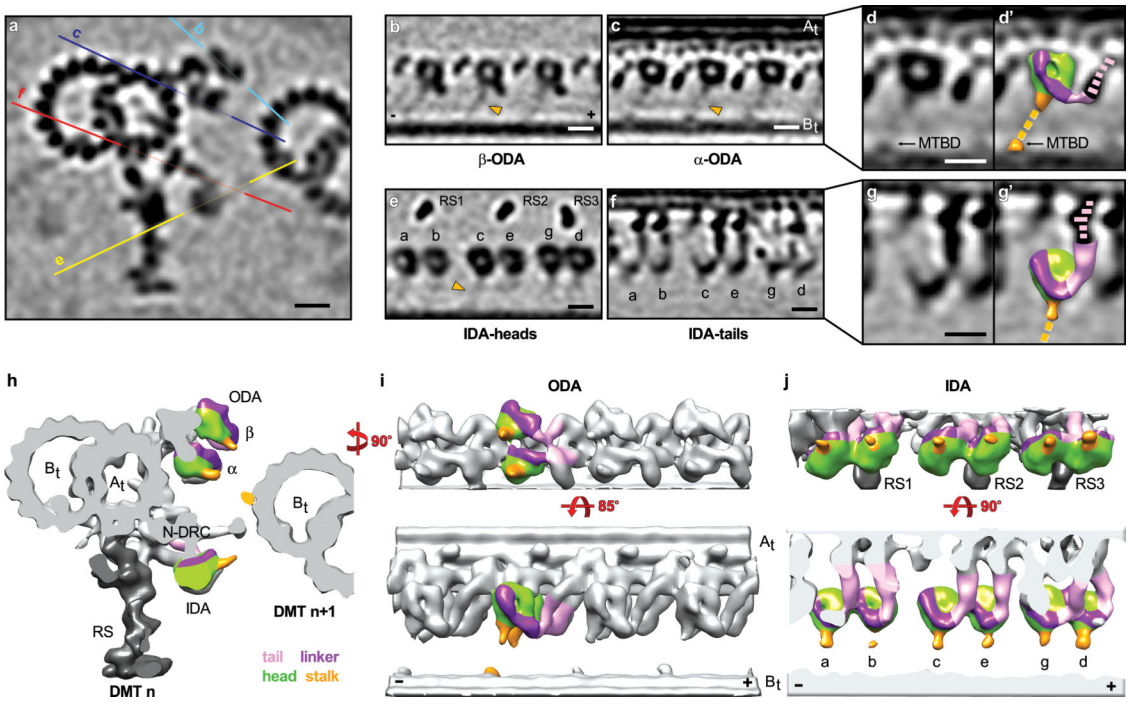

Figure 2.

In situ structures of sea urchin axonemal dyneins in the post-powerstroke state as revealed by cryo-ET. (**a**) Tomographic slice of an averaged axonemal 96 nm repeat, viewed in cross-section from the proximal side, showing the *in situ* arrangement of axonemal dyneins. Coloured lines indicate locations of tomographic slices shown in **b, c**, **e**, and **f**. (**b**-**g**) Longitudinal tomographic slices of averaged axonemal dyneins. **d**/**d’** and **g**/**g’** are magnifications of **c** and **f**. In **d’** and **g’**, isosurface-rendered 3D images of averaged α-ODA and IDA dynein c are superimposed onto corresponding tomographic slices in **d** and **g**. (**h**-**j**) 3D isosurface renderings of averaged axonemal dyneins. Tail (pink), linker (magenta) and head (green) domains are clearly visible in both tomographic slices and isosurface renderings; coiled-coil stalks (orange arrowheads) are distinct in the tomographic slices (**b**, **c**, **e**). Other labels: doublet microtubule (*DMT*), A-tubule (A_t), B-tubule (B_t), microtubule binding domain (*MTBD*), nexin-dynein regulatory complex (*N-DRC*), radial spoke (*RS*), microtubule polarity (+ and - end). Structure-colour coding is preserved in isosurface renderings throughout all figures. Scale bars: 10 nm.

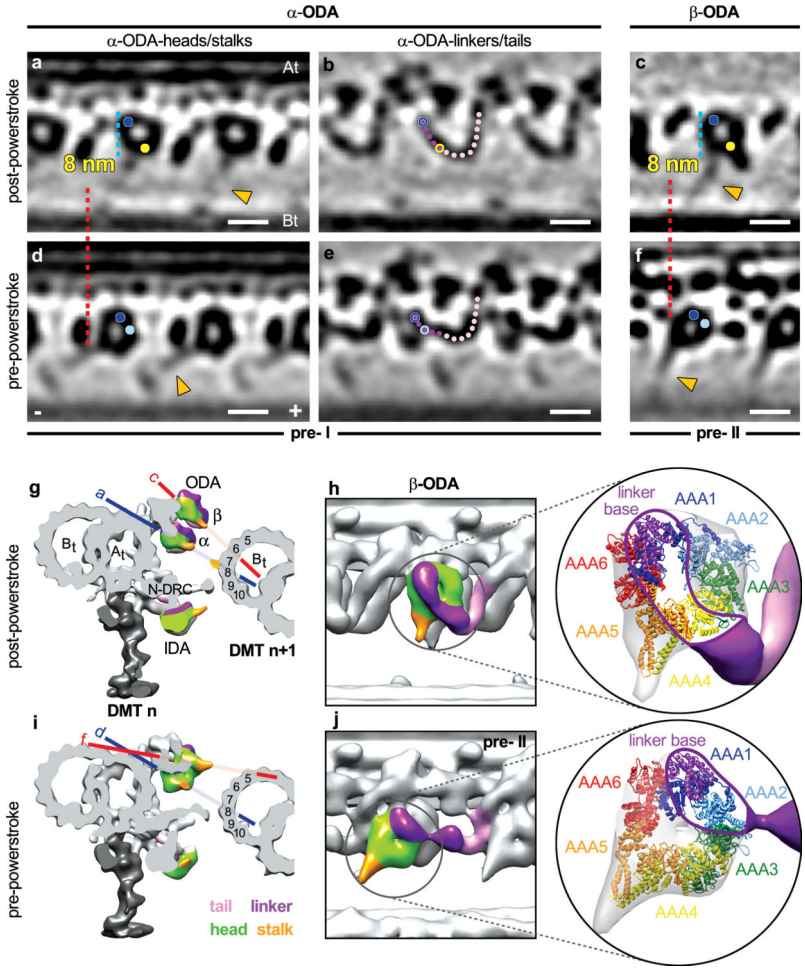

Figure 3.

In situ structural changes of ODAs between post- and pre-powerstroke states. (**a-f**) Longitudinal tomographic slices of averaged axonemal dyneins in post- (**a-c**), pre-I (**d**, **e**) and pre-II (**f**) powerstroke states; note the difference in curvature of the stalks (orange arrowheads). Coloured dots and rings in **a-f** indicate interaction sites of the linker with specific AAA domains of the dynein heads: AAA1 (dark blue), AAA2 (light blue), AAA4 (yellow); in **b** and **e** linker and tail are indicated with magenta and pink dots, respectively. (**g-j**) 3D isosurface renderings of DMT in cross-view (**g**, **i**) and the conformational changes of the ODAs between post-powerstroke (**h**) and pre-powerstroke states (**j**). Coloured lines (**g**, **i**) indicate the orientation of the tomographic slices (**a**, **c**, **d**, **f**); protofilaments numbered according to Linck and Stephens[31]. Interactions between the linker and head are shown by docking the crystal structure of *S. cerevisiae* cytoplasmic dynein (ribbon representation with AAA1-6 from PDB 4AKI)[12] into our EM volume (insets in **h**, **j**); note the linker base that connects to AAA1. Other labels: A-tubule (A_t), B-tubule (B_t), doublet microtubule (DMT), nexin-dynein regulatory complex (*N-DRC*). Scale bar: 10 nm.

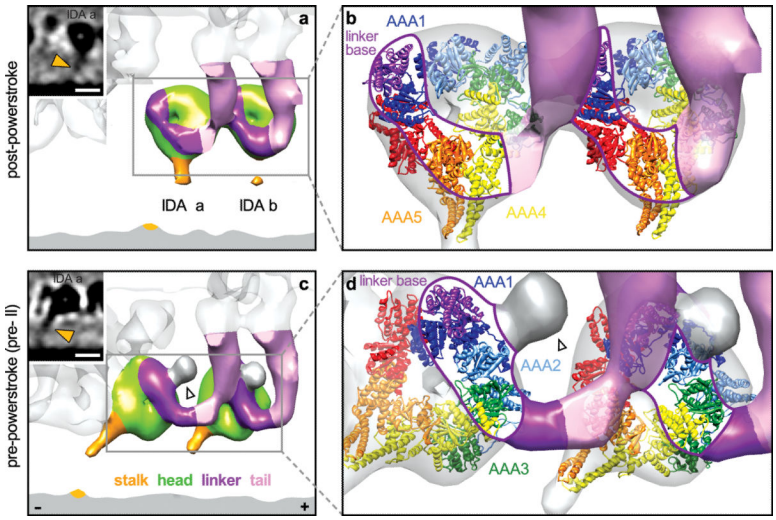

Figure 4.

In situ structural changes of IDAs between post- and pre-powerstroke states. (**a-d**) 3D isosurface renderings of averaged IDAs in post-powerstroke (**a**, **b**) and pre-powerstroke states (**c**, **d**). Insets show the different curvature of the stalks (orange arrowheads) in the tomographic slices of IDA a. In **b** and **d** the crystal structure of *S. cerevisiae* cytoplasmic dynein (ribbon representation with AAA1-6 from PDB 4AKI)[12] is docked into our IDA EM volumes, illustrating changes in the interaction between the linker and head. White arrowheads in **c** and **d** highlight an extra density that specifically attaches to the linker, AAA1 and 2 in pre-powerstroke states. Scale bar: 10 nm (inset **a**, **b**).

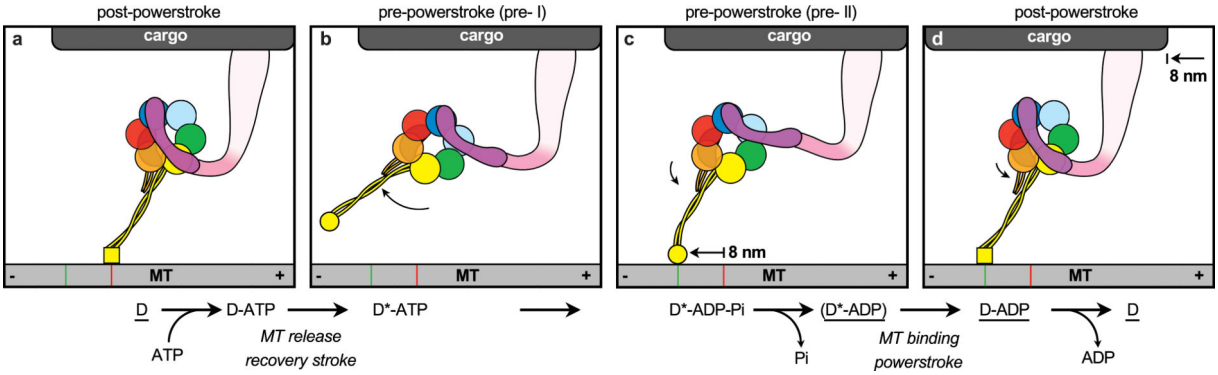

Figure 5.

Schematic model of dynein movement. (**a-d**) Schematics of dynein in post-(D) and pre-powerstroke (D*) conformations observed by cryo-ET; the interpretation of the nucleotide state of the conformations is based on previous kinetic studies[3-5]. Underlined dynein states (D, D*-ADP, D-ADP) are predicted to have strong microtubule affinity. For a detailed explanation, see text. Other labels: microtubule polarity (+ and - end), microtubule (*MT*), red lines: location before step, green lines: location after one step.